Article

Atomically engineering metal vacancies in monolayer transition metal dichalcogenides

Check for updates

Xiaocang Han[1,11], Mengmeng Niu[2,11], Yan Luo[3,11], Runlai Li [4], Jiadong Dan[5], Yanhui Hong[6], Xu Wu[2], Alex V. Trukhanov[7], Wei Ji [8], Yeliang Wang[2], Jiahuan Zhou[9], Jingsi Qiao[2] ✉, Jin Zhang [1] ✉ & Xiaoxu Zhao [1,10] ✉

Scanning probe microscopy and scanning transmission electron microscopy (STEM) are powerful tools to trigger atomic-scale motions, pattern atomic defects and lead to anomalous quantum phenomena in functional materials. However, these techniques have primarily manipulated surface atoms or atoms located at the beam exit plane, leaving buried atoms, which govern exotic quantum phenomena, largely unaffected. Here we propose an electron-beam-triggered chemical etching approach to engineer shielded metal atoms sandwiched between chalcogen layers in monolayer transition metal dichalcogenide (TMDC). Various metal vacancies (V_{MX_n}, $n = 0-6$) have been fabricated via atomically focused electron beam in STEM. The parent TMDC surface was modified with surfactants, facilitating the ejection of sandwiched metal vacancies via charge transfer effect. In situ sequential STEM imaging corroborated that a combined chemical-induced knock-on effect and chalcogen vacancy-assisted metal diffusion process result in atom-by-atom vacancy formation. This approach is validated in 16 different TMDCs. The presence of metal vacancies strongly modified their magnetic and electronic properties, correlated with the unpaired chalcogen p and metal d electrons surrounding vacancies and adjacent distortions. These findings show a generic approach for engineering interior metal atoms with atomic precision, creating opportunities to exploit quantum phenomena at the atomic scale.

The ability to manipulate and engineer atomic structures and dynamics is driving us closer to one of the ultimate goals (the precise control over matter at the atomic scale) in nanoscience and nanotechnology[1,2]. With rapid instrument progress in scanning probe microscopy[3], patterning and controlling atoms with atomic precision has been realized, including creating new states of matter *via* scanning tunnelling microscopy, ranging from low-dimensional Dirac materials (such as artificial electronic lattices of molecular graphene[4] and Lieb lattice[5,6]) and electronic quantum fractals[7], to complex magnetic order[2]. Despite great successes being achieved by scanning tunnelling microscopy over

[1]School of Materials Science and Engineering, Peking University, Beijing, China. [2]MIIT Key Laboratory for Low-Dimensional Quantum Structure and Devices & Advanced Research Institute of Multidisciplinary Science, Beijing Institute of Technology, Beijing, China. [3]Frontiers Science Center for Flexible Electronics and Institute of Flexible Electronics, Northwestern Polytechnical University, Xi'an, China. [4]College of Polymer Science and Engineering, State Key Laboratory of Polymer Materials Engineering, Sichuan University, Chengdu, China. [5]NUS Centre for Bioimaging Sciences, National University of Singapore, Singapore, Singapore. [6]DP Technology, Beijing, China. [7]SSPA 'Scientific and Practical Materials Research Centre of NAS of Belarus', Minsk, Belarus. [8]Beijing Key Laboratory of Optoelectronic Functional Materials & Micro-Nano Devices, Department of Physics, Renmin University of China, Beijing, China. [9]Wangxuan Institute of Computer Technology, Peking University, Beijing, China. [10]AI for Science Institute, Beijing, China. [11]These authors contributed equally: Xiaocang Han, Mengmeng Niu, Yan Luo. ✉e-mail: qiaojs@bit.edu.cn; jinzhang@pku.edu.cn; xiaoxuzhao@pku.edu.cn

the past few decades, the techniques are limited to relatively weakly bound surface adatoms or vacancies, cryogenic temperature and low throughput[8,9], which hinders the engineering of a large array of nanostructures. Another paradigm of building structures atom-by-atom has recently emerged via subangstrom focused electron beam (e-beam) in scanning transmission electron microscopy (STEM)[10–12], such as sculpting metallic patterns (atomic chains, or membranes) in two-dimensional (2D) semiconducting transition metal dichalcogenide (TMDC) monolayers and building an atomic level seamless Ohmic contact[13,14]. The three-atom-thick structure matrix of TMDC offers an optimum template to position the electron probe onto single atoms with elemental identity and induce precise alterations[15]. Manipulating atoms via STEM in TMDCs can, for example, create single chalcogen vacancies, trigger novel phase formations and transform the composition of layered materials in places with atomic precision[14,16–18]. The engineering of atomic structures has been largely confined to surface chalcogen atoms and associated vacancy complexes due to their relatively low formation energy[19–22]. Despite the structure of TMDCs being mainly unaffected after losing chalcogen atoms in the outmost layer, an expansive property space (such as optical emission, conduction behaviour and magnetism) can be spatially tailored via modification of their basal surfaces and associated electron states[23–26]. However, knocking out single interior metal atoms via focused impinging e-beam has rarely been realized, even in one-layer three-atom-thick TMDC materials[10,13].

Knocking out interior metal atoms significantly perturbs the backbone of the atomic structure and rehybridizes the electronic structures of TMDCs, potentially creating interesting physical and chemical properties, which the pristine lattice rarely possesses[27–29]. For example, transforming non-magnetic to magnetic 2D materials can be realized by introducing magnetic metal vacancies. Pt vacancies in non-magnetic monolayer $PtSe_2$ (ref. [29]) account for the antiferromagnetism, which stems from defect-induced spin-split states that emerge at the Fermi level. Besides, the metal vacancy complex (V_{WSe_6}) combined with internal strain in monolayer WSe_2 has been demonstrated to be optically conductive, enabling single-photon emission with high purity up to 150 K (ref. [17]). V_{MoS_6} vacancy complexes in monolayer MoS_2 can effectively reject ions and allow water transport at a high rate for water desalination, as revealed by molecular dynamics simulations[30]. However, forming metal vacancies is thermodynamically and kinetically challenging compared to the corresponding chalcogen counterparts, since the metal atomic layer was sandwiched between and protected by the top and bottom two chalcogen atomic layers. Therefore, collectively forming large-scale metal vacancies in TMDC monolayers remains elusive.

Ion (Ga^+, He^+)-beam lithography has been utilized to fabricate complex metal-chalcogen vacancies, such as $V_{MoS_n(n=3-6)}$ or nanometre vacancies with multi-metal atoms in MoS_2 and WS_2 (refs. [28,31]). Despite the large density of atomic defects being formed, large irregular vacuum holes together with severe sample damages are associated with the ion-beam irradiation[31]. More importantly, the defect formation via the ion beam approach cannot be in situ monitored and precisely controlled. Therefore, developing a reliable and highly reproductive approach to in situ and selectively induce metal vacancies in the TMDC family is challenging. The correlation between atomic-scale defect features and associated property modifications is interesting and awaits investigation in monolayer TMDCs.

In this work, we propose a universal e-beam-induced chemical etching method and successfully fabricate buried metal vacancies (V_M) and associated metal vacancy complexes (V_{MX_n}) in monolayer TMDCs by STEM. An atlas of metal vacancies has been sculpted and in situ atomically identified in 16 different monolayer TMDCs exhibiting distinct polymorphs (1H, 1T, 1T' and 1T''), suggesting this approach is generic and highly reproducible. Monolayer TMDC flakes are exfoliated by a polymer-assisted electrochemical method. We find that the surface capping of organic molecules is significant, lowering the knock-on

threshold of the buried metal atom in the MX_2 monolayer regardless of their atomic and electronic structures. The combined capping molecules–TMDCs interaction and chalcogen vacancy-assisted metal diffusion process are responsible for forming metal vacancies, as corroborated by STEM and density functional theory (DFT). As suggested by DFT calculations, local magnetic moments (-1.23–4.36 μ_B) are found in monolayer $MoSe_2$, attributed to the unpaired d/p electrons localized at the nearest-neighbour M/X atoms that surround the metal vacancies and strongly related to the local distortions. Our results make a step forward for controlling buried atoms away from the surface and open a new avenue to engineer electronic properties of TMDCs via metal vacancy engineering, in which a library of interesting properties awaits exploration.

Results and discussion
Fabrication of metal vacancies in TMDC monolayers

We first unveil the metal vacancies in 1H-NbS_2 monolayer as an example to demonstrate the introduction of metal vacancies via e-beam-induced chemical etching method, as illustrated in Fig. 1a. Metallic NbS_2 monolayer was selected because of its relatively simple e-beam damaging channel. The complex ionization effect in metallic materials is negligible due to a rapid electron–hole pair recombination process upon e-beam irradiation[32], leaving a dominant ballistic knock-on effect and chemical etching effect (Supplementary Information). Monolayer NbS_2 flakes were exfoliated by a polymer-assisted electrochemical cathodic exfoliation method[33], where tetrahexylammonium cation (THA) and polyvinylpyrrolidone (PVP) polymers served as intercalants and surfactants, respectively. The electrochemical setup for the electrochemical cathodic exfoliation method is displayed in Fig. 1a (left). NbS_2 single crystals were used as the cathode, and Pt wire served as a counter electrode. By applying a negative bias, THA and PVP molecules were gradually driven into the van der Waals gaps of NbS_2 crystals, resulting in gentle expansion and therefore exfoliated 2D flakes upon gentle mechanical shaking. The freshly exfoliated monolayer NbS_2 flakes were immediately passivated by PVP molecules, as confirmed by a relatively higher contrast in annular dark field scanning transmission electron microscopy (ADF-STEM) images (Fig. 1b and Supplementary Figs. 1 and 2) together with signature N signals as further corroborated by energy-dispersive X-ray spectroscopy (EDS) (Fig. 1d).

The capping PVP agent is prerequisite to induce metal vacancies via the e-beam sculpting approach, as discussed later. Upon e-beam irradiation of ~10^7 e^- nm^{-2} during STEM imaging, a few individual metal vacancies are generated in PVP-capped 1H-NbS_2 (Fig. 1c and Supplementary Fig. 3), in contrast to the solely e-beam-induced chalcogen vacancies in clean TMDCs[15,19]. Notably, the metal vacancies formation process was accompanied by the creation of a large number of S vacancies (Supplementary Fig. 3) and possible PVP radiolysis[32], as illustrated in Fig. 1a (right). Because of the metallic nature of the 1H-NbS_2, the ionization effect, being responsible for creating large irregular nanopores via a complete ionization of chalcogen (X) and metal (M) atoms in semiconducting and insulating materials[13], is unlikely to be the predominant mechanism. Regarding the other prevalent knock-on effect, the displacement threshold of Nb atoms is significantly larger than the maximum energy transferred from a 60 kV e-beam[21], suggesting that pure knock-on damage is most unlikely to dominate either. Interestingly, the metal vacancy verified by the vacuum hole occupying the centre of the hexagon composed of the nearest metal sites is located within the polymer-passivated area (Fig. 1c), indicating that the polymer could play a pivotal role in assisting metal vacancy formation. Sequential STEM imaging (Fig. 1e,f) shows that once a metal atom was ejected, it rapidly redeposited onto the adjacent surface area (Supplementary Fig. 4). A close examination (Fig. 1f) reveals that the creation of metal vacancies may involve the loss of neighbouring S atoms, presumably associated with a combined knock-on and chemical etching effect. In addition, we found that only isolated metal vacancies (Fig. 1g) and
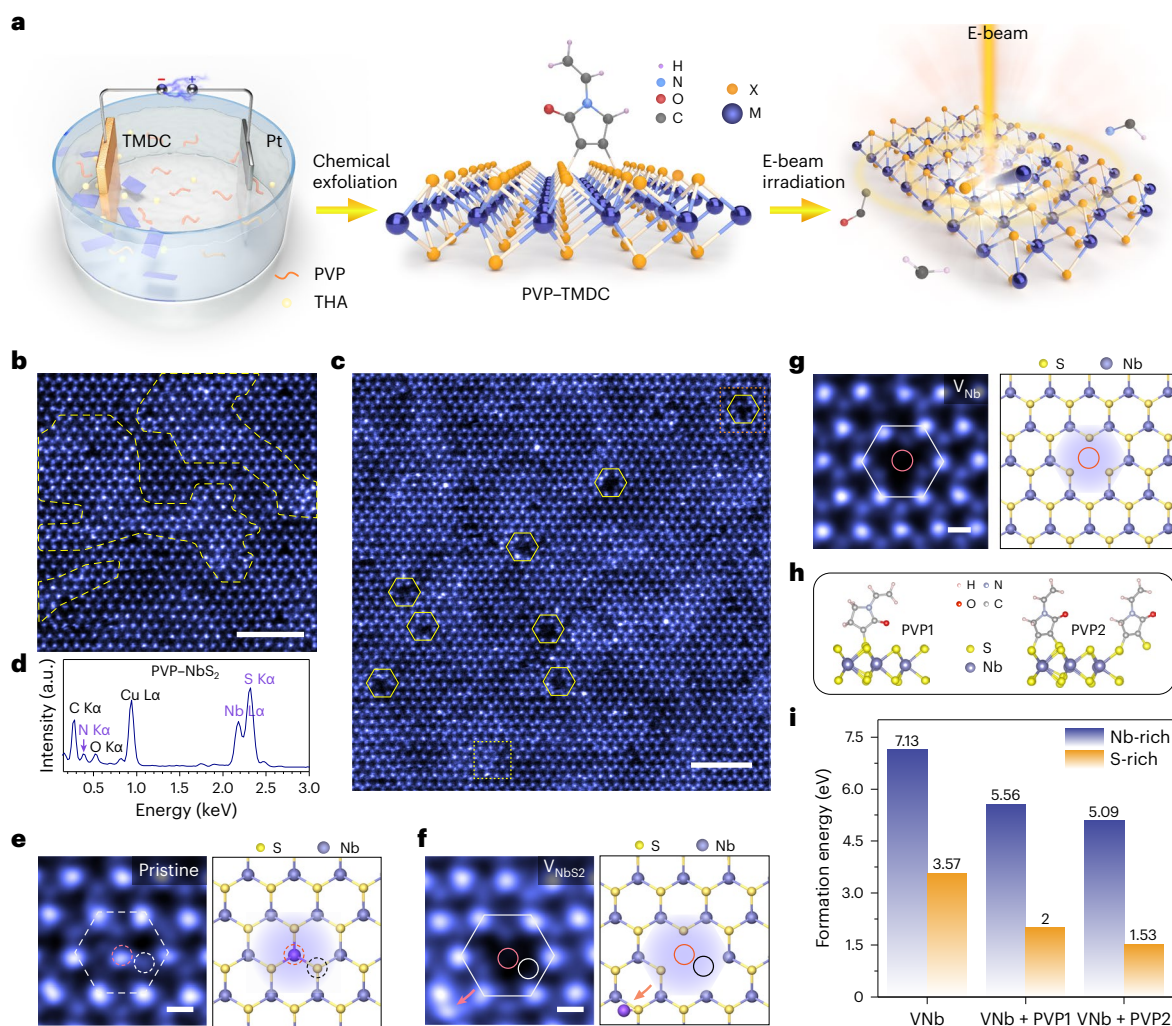
Fig. 1 | Forming metal vacancies via chemical-induced knock-on effect. a, Schematic illustration showing the formation of PVP-capped TMDC monolayers, and subsequent metal vacancy formation via e-beam-induced chemical etching knock-on effect. In the chemically exfoliated process, THA and PVP polymers are serving as intercalants and surfactants, respectively. **b,c,** Atomic-resolution medium-angle ADF-STEM image of pristine monolayer 1H-NbS$_2$ (**b**) and monolayer 1H-NbS$_2$ containing a few Nb vacancies upon e-beam irradiation (**c**). The collection angle of the medium-angle ADF images ranges from 30 mrad to 110 mrad. **d,** EDS spectrum of chemically exfoliated PVP-capped monolayer 1H-NbS$_2$. **e,f,** Sequential ADF-STEM images showing the birth of a single Nb metal vacancy together with a pair of adjacent S dimers vacancies at the same region. In **e** and **f,** the corresponding atomic models are depicted on the right. **g,** ADF-STEM image displaying a single Nb metal vacancy and its corresponding atomic model is depicted on the right. **h,** DFT-calculated atomic models of PVP-capped 1H-NbS$_2$. **i,** DFT-calculated formation energies of metal vacancy in pristine and PVP-capped 1H-NbS$_2$ under metal (Nb)- or chalcogen (S)- rich conditions. Scale bars: 2 nm (**b** and **c**) and 0.2 nm (**e**–**g**).

metal vacancy complexes (Fig. 1f) were created, and no large irregular vacuum holes were generated upon a prolonged e-beam irradiation (Supplementary Fig. 5) as frequently observed in semiconducting or insulating 2D materials. Therefore, these results suggest that the metal vacancy formation in monolayer NbS$_2$ strongly correlates to the synergetic beam-induced chemical etching mechanism assisted by capping PVP molecules.

To further elucidate the underlying damaging mechanisms, we performed DFT calculations. The formation energy of metal vacancy in PVP-capped NbS$_2$ was first assessed (Fig. 1h,i). As a strong capping agent, PVP–1H-NbS$_2$ interaction models were calculated on the basis of the dehydrogenation number (Fig. 1h). Comparing the high energy needed for ejecting one metal atom in clean 1H-NbS$_2$, the charge transfer[33,34] from chemisorbed molecules[35] substantially reduces the formation energy by nearly half under chalcogen-rich conditions (Fig. 1i). The calculations indicate that the formation of such PVP–S$_2$-Nb structure is probably associated with the changes in the Nb knock-on thresholds upon adding PVP molecules onto the NbS$_2$ surface. Thus,

the e-beam-induced metal vacancy formation is believed to be predominantly triggered by the synergistic effect from both chemical etching and ballistic displacement, where we term this mechanism as the chemical-induced knock-on effect. Besides, the primary role of the e-beam is to provide energy to overcome the relatively low binding energy of Nb–S bonds due to the charge transfer from capping PVP molecules.

Atomic vacancy structures and formation dynamics

Not only pure metal vacancies were produced upon e-beam irradiation, but rich metal vacancy complexes (V$_{MX_n}$, $n = 1$–6) containing distinct adjacent chalcogen vacancies were created in monolayer 1H-NbS$_2$ (Fig. 2). Figure 2a displays seven typical metal vacancies, including mononiobium vacancy (V$_{Nb}$), vacancy complexes of one Nb and monosulfur (V$_{NbS}$), one disulfur pair (V$_{NbS_2}$), three sulfur (V$_{NbSSS}$), two disulfur pairs (V$_{NbS_2S_2}$), five sulfur (V$_{NbS_2S_2S}$), and three disulfur pairs (V$_{NbS_2S_2S_2}$), where V$_{NbSSS}$ represents losing three S atoms at different S pairs, and subscript 2 denotes the loss of one S pair. In parallel, their corresponding atomic
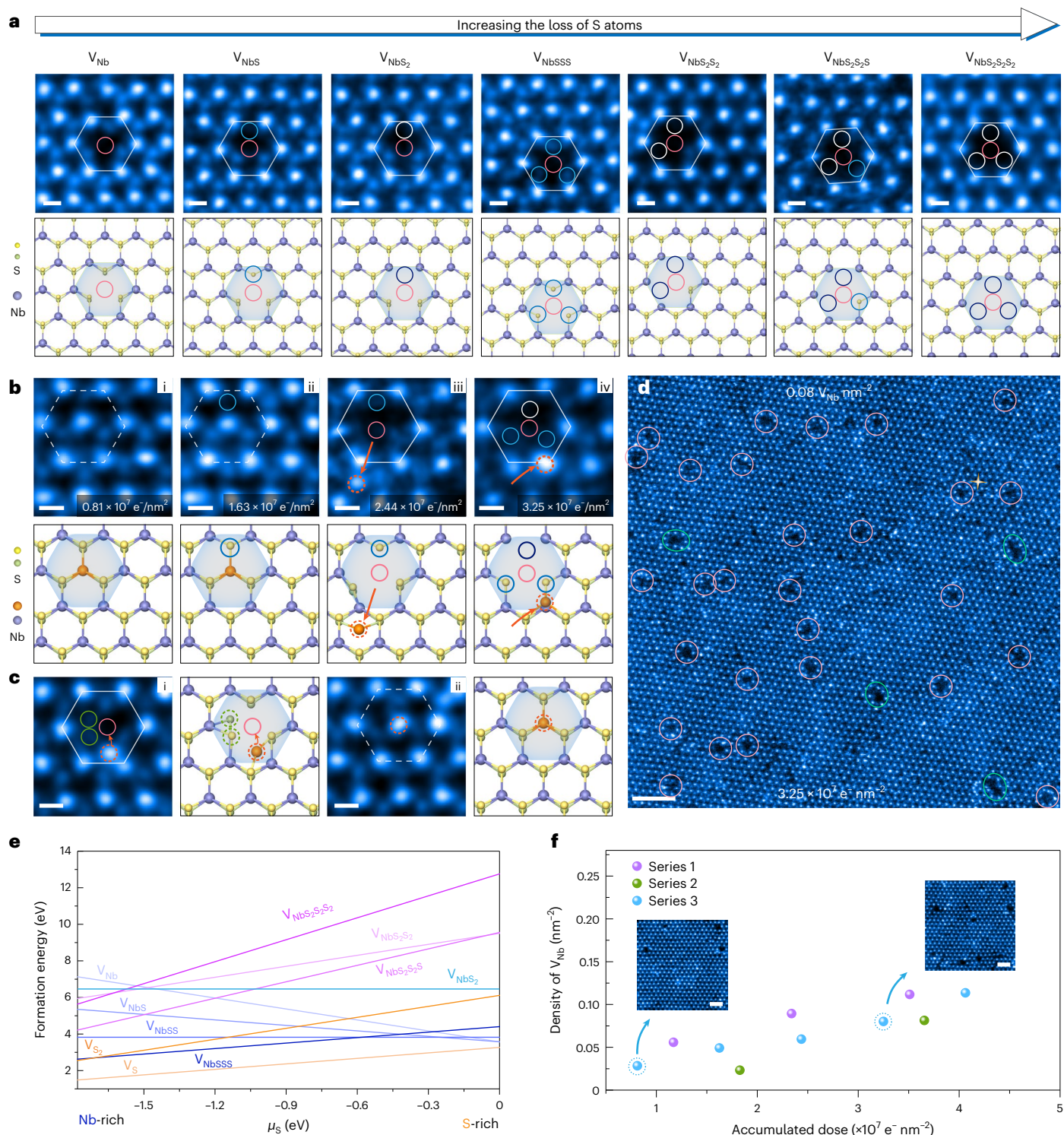
Fig. 2 | Atomic structures and associated dynamics of metal vacancies.
a, Atomic-resolution ADF-STEM images showing the detailed configurations of seven types of Nb metal vacancies in monolayer NbS$_2$. The lower panels display their corresponding atomic models. **b**,**c**, Sequential STEM images (i–iv) at the same region showing a step-by-step metal vacancy formation mechanism (**b**) and vacancy self-healing process (**c**). Blue, white (dark blue) and pink solid circles inside hexagon frames represent the removal of one S, a pair of S, and

single Nb atoms, respectively. The pink dotted circles represent the relocating (**b**) or refilling (**c**) behaviours of sputtering single Nb atom. **d**, Wide-scan STEM image showing the distribution of metal vacancies. Single metal vacancies and subnanopores are denoted by pink and green circles, respectively. **e**, DFT calculated formation energies of various Nb vacancy complexes as a function of S chemical potential. **f**, Statistical analysis of metal vacancy density as a function of e-beam irradiation dose. Scale bars: 0.2 nm (**a**–**c**), 2 nm (**d**) and 1 nm (**f**, inset).

models are depicted in the lower panels of Fig. 2a. The Z-contrast nature of ADF-STEM imaging enables us to distinguish the monosulfur vacancy (V$_{NbS}$) from disulfur vacancy (V$_{NbS_2}$) by quantitative analysis of the image intensity (Supplementary Fig. 6)[36]. After surveying 85 flakes, we found

that single metal vacancies are occasional, and neighbouring S vacancies are usually accompanied (Supplementary Fig. 5).

Next, we employed sequential ADF-STEM imaging (Fig. 2b) to further unveil the dynamics of a metal vacancy from birth to evolution.

The results reveal that one S atom was initially knocked out by the impinging electrons, considerably decreasing the stability of the neighbouring bonded Nb atoms. Subsequently, the incoming high-energy electrons bombarded the unsaturated Nb atoms located at the beam exit plane, escaping from their pristine position accompanied by PVP radiolysis and relocated onto the nearby NbS_2 surface (Fig. 2b and Supplementary Fig. 4). The ejected Nb atom is highly mobile upon e-beam irradiation (Supplementary Fig. 7), and it may occasionally refill the vacancy and heal the NbS_2 lattice when the knock-out Nb is nearby (Fig. 2c). Statistically, single metal vacancies (V_{Nb}) are occasionally found in NbS_2 after surveying abundant datasets, and their creation probably involves the S vacancy refilling as verified by the in situ recovering of S vacancy (Supplementary Fig. 7). Once Nb vacancy is created, it further reduces the displacement threshold of adjacent S atoms[37]. Therefore, Nb vacancies consecutively developed into Nb vacancy complexes containing various S vacancies upon a prolonged e-beam irradiation.

The thermodynamic stabilities of a series of metal vacancies are further examined by theoretical calculations (see the definition in Methods). The metal vacancy formation energy as a function of S chemical potential, spanning from Nb-rich to S-rich, is calculated by DFT and plotted in Fig. 2e. Single S vacancy is the predominant defect type as it is the most thermodynamically stable configuration in both Nb-rich and S-rich condition, consistent with the ADF-STEM results, ~0.96 V_S nm^{-2} at a dose of 4×10^7 e^- nm^{-2} (Supplementary Fig. 5). S vacancies at different electron doses can be located efficiently and precisely via deep learning (Supplementary Fig. 8), where the deep learning model is trained on the basis of fully convolutional networks (FCNs) with ResUNet architecture[38]. The formation energy of V_{NbS_n} is relatively high, in line with the experimental results that a low V_{MX_n} density (<0.12 nm^{-2}) is consistently observed in experiments. Pink circles in Fig. 2d highlight the single metal vacancy complexes with a concentration of 0.08 V_{NbS_n} nm^{-2} at a total dose of 3.25×10^7 e^- nm^{-2}. Nb vacancy density is linearly proportional to the total electron dose (Fig. 2f), as demonstrated by a series of low-magnified STEM images (Supplementary Fig. 5). Notably, metal vacancy complexes with variable S vacancies are produced simultaneously (Supplementary Figs. 5 and 9), whereas V_{NbS}, V_{NbSS} and V_{NbSSS} take up a large proportion in single metal vacancy complexes, consistent with the DFT calculations. On the other hand, subnanometre pores with irregular size and shape were generated and annihilated under prolonged e-beam irradiation but increased when the dose was higher than 3.25×10^7 e^- nm^{-2} (Fig. 2d and Supplementary Fig. 5).

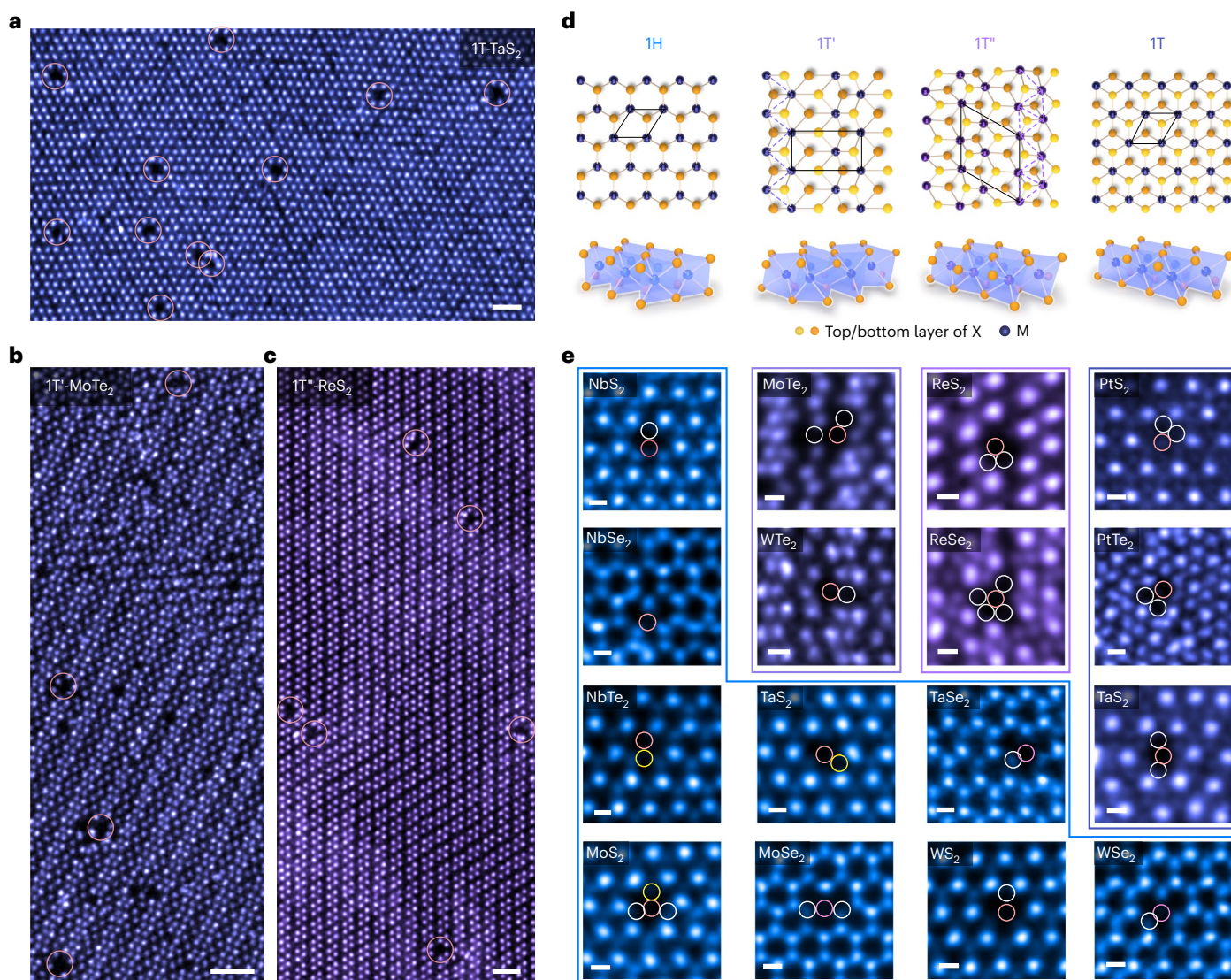**Fabricating metal vacancies in various monolayer TMDCs**

The chemical-induced knock-on effect has been demonstrated as an effective approach to selectively generate Nb vacancies in $1H$-NbS_2. To further test the validity in other TMDC monolayers, we exfoliated an additional 15 types of monolayer TMDCs exhibiting distinct polymorphs, including 1H, 1T, 1T′ and 1T″ phases (Fig. 3), using the same method, and the results are shown in Fig. 3 and Supplementary Figs. 10–21. Not only metallic TMDC monolayers were tested, semiconducting, semi-metallic thin films were also verified. Notably, almost all single metal vacancy complexes with varying chalcogens V_{MX_n} ($n = 0$–6) have been consistently fabricated regardless of polymorphs and conductivity, including $1H$-NbS_2, $1H$-$NbSe_2$, $1H$-$NbTe_2$, $1H$-MoS_2, $1H$-$MoSe_2$, $1T′$-$MoTe_2$, $1H$-TaS_2, $1T$-TaS_2, $1H$-$TaSe_2$, $1H$-WS_2, $1H$-WSe_2, $1T′$-WTe_2, $1T″$-ReS_2, $1T″$-$ReSe_2$, $1T$-PtS_2 and $1T$-$PtTe_2$. In parallel, atomic-resolution STEM images (Fig. 3a–c) of polymer-passivated 1T, 1T′ and 1T″ phases further confirmed that the metal atoms displaced from the pristine lattice and relocated onto the nearby TMDC surface. After statistically counting metal vacancies in 16 different TMDC monolayers, we seldomly observe single metal vacancies (V_M) (Fig. 3e), suggesting that forming chalcogen vacancy is the prerequisite to trigger subsequent metal vacancy to some extent[15].

Metal vacancies in semiconducting TMDCs were less controllable. Large holes are readily created because a mass of X and M atoms are ionized simultaneously in semiconducting flakes (Supplementary Fig. 22). On the other hand, atom-by-atom knock-on event dominates in metallic film (Supplementary Fig. 5). Nevertheless, PVP capping decreases the formation energy in semiconducting TMDCs via the same charge transfer effect (Supplementary Fig. 23). Both ionization damage and chemical etching contribute to the damaging channel in semiconducting flakes[39]. In the STEM observations of semiconducting $1H$-$MoSe_2$, most Mo vacancies are present as defect complexes of V_{MoSe_3} composed of V_{MoSeSe} and V_{MoSe_2Se} (Supplementary Fig. 22). Statistically, other V_{MoSe_n} complexes were observed less frequently, especially configurations containing Se pairs (Supplementary Fig. 24) presumably owing to their thermodynamic instability with more unsaturated coordination environments. Consistently, single V_{Mo} is rarely observed, that is the result of proposed kinetic formation path and verified by our theoretical calculations (Supplementary Fig. 25). The DFT results show that the formation energy of V_{Se} (1.8 eV) is substantially higher than the vacancies next to V_{Mo} (-0.9 eV), suggesting that, once V_{Mo} is created, the adjacent Se atoms become highly volatile to e-beam irradiation, prone to form V_{MoSe_n} ($n > 0$).

Among TMDC polymorphs, the distorted octahedral (1T′ and T″) phases show unique superstructures of 1×2 (1T′) and 2×2 (T″) and distinctive in-plane anisotropic properties, which consist of transition metal zigzag chains (1T′) and diamond-like shape (T″) (Fig. 3d and Supplementary Figs. 18 and 20). After analysing the exact sites of metal vacancies, two non-equivalent metal sites (M_n, $n = 1, 2$) and four non-equivalent X sites (X_n, $n = 1, 2, 3, 4$), statistic counting results reveal that vacancies are prone to occur at M_1 and X_4 site in anisotropic 1T″ TMDCs (Supplementary Figs. 20 and 21) owing to the relatively stronger M_2–M_2 bonding and larger space volumes at X_4 sites[40]. However, no notable preferences were found in 1T′ TMDCs (Supplementary Figs. 19 and 20) since the metal sites in 1T′ have similar coordination environments and the formation of X vacancy is attributed to the combined effect of deformation (ripple) and anisotropic lattice bonding[41]. The feasibility and validity of e-beam-triggered chemical etching approach to bilayer TMDCs is also verified (Supplementary Figs. 26 and 27), and metal vacancies can be routinely fabricated.

Magnetic properties of metal vacancies in monolayer TMDCs

We have successfully created a wide range of vacancies in monolayer TMDCs through the beam-etching irradiation method, especially single metal vacancy complexes. The loss of metal atoms significantly disrupts the local electronic structure and magnetic moment, which provides us with opportunities to discover novel physical phenomena. Therefore, we further investigated the electronic and magnetic properties of various vacancies in monolayer $MoSe_2$ using first-principles calculations. Figure 4 illustrates the spin density and local magnetic moment evolution from V_{Mo} to V_{MoSe_6} in monolayer $MoSe_2$ (Supplementary Fig. 28). Except V_{Mo} and V_{MoSe}, the local magnetic moment gradually increases when additional Se atoms are lost adjacent to the Mo vacancy site, and the total magnetic moment can reach 4.36 μ_B in $V_{MoSe_2Se_2Se_2}$ (Fig. 4c). V_{Mo} and V_{MoSe} prefer a spin polarization located on the nearest Se (50.7%, 48%) and next-nearest neighbouring Mo (40.4%, 44.7%) atoms (Fig. 4b,c), contributed by the unsaturated Se dangling bond around the Mo vacancy site (Supplementary Fig. 28). Spin density distribution illustrated that the magnetic moments in $V_{MoSe_{3-6}}$ are mainly contributed by the exposed Mo atoms and the next-nearest neighbouring Mo atoms (Fig. 4a and Supplementary Fig. 28). The metal vacancy complexes configuration in monolayer $MoSe_2$ was further corroborated by the simulated image (Supplementary Fig. 29). Losing one Se dimer (V_{MoSe_2}) is prone to induce magnetic moment in metal vacancies (Supplementary Table 1) compared with losing two Se at different sites (V_{MoSeSe}). The calculated spin-up and spin-down projected density of states show non-degenerated

Fig. 3 | Generic fabrication of metal vacancies in an atlas of monolayer TMDCs. a–c, Atomic-resolution ADF-STEM images showing the metal vacancy complexes generation in 1T-TaS$_2$ (a), 1T'-MoTe$_2$ (b), and 1T''-ReS$_2$ (c) phases triggered by e-beam irradiation. d, Atomic models of 1H, 1T, 1T' and 1T'' phases. e, ADF-STEM images of the as-fabricated 1H, 1T, 1T' and 1T'' TMDCs containing various metal vacancies. V$_M$, V$_X$ and V$_{X_2}$ vacancies in e are highlighted by pink, white and yellow circles, respectively. Scale bars: 1 nm (a–c) and 0.2 nm (e).

characteristics, which further indicate that the magnetic moment of V$_{MoSe_{0-6}}$ originates from the hybridization between Mo 4d and Se 4p states, particularly from the unpaired spin polarization states with asymmetric projected density of states between the spin-up and spin-down near the Fermi surface (Supplementary Figs. 30 and 31). In addition, the electronic structures of defective MoSe$_2$ vary from semiconductor to half-metal, which is largely determined by the local configurations of V$_{MoSe_{0-6}}$ (Supplementary Figs. 30 and 31). The introduction of magnetic moments via metal vacancies in various TMDCs has also been confirmed (Supplementary Figs. 32–34 and Supplementary Table 2).

Considering the interplay between mechanical deformation and magnetic behaviour[42], it was predicted that the local strain induced by metal vacancy considerably impacts the magnetic properties of TMDCs[43]. The strong local lattice distortion around the metal vacancy is elucidated in Fig. 4b and Supplementary Figs. 35–37. Interestingly, only the introduction of a metal vacancy (V$_{Mo}$) in the MoSe$_2$ monolayer accompanied by nearest X–X constriction is likely to give rise to the magnetic moment, whereas V$_M$ in MoS$_2$ or WSe$_2$ contributed to the

nearest X–X expansion does not present any intrinsic spin polarization (Fig. 4b and Supplementary Figs. 31 and 35). Especially, three pairs of Se around the V$_{Mo}$ vacancy in the MoSe$_2$ monolayer move towards the vacancy centre and form a triangle, whereas the next-nearest Mo atoms move away (1%) from the vacancy centre (Fig. 4b and Supplementary Fig. 35). The distances between the neighbouring Se pairs decrease from 3.30 Å to 3.18 Å, and the local contraction strain is estimated to be 4%. This leads to a strong magnetic exchange interaction between the nearest Se pairs, which is greater than the adjacent Mo–Se bonding energy and results in spin polarization at nearby atoms. The change of interatomic X–X and M–M distances in V$_{MX_n}$ is consistently and widely observed around the metal vacancy, exhibiting a maximum deviation of tens of picometres correlated to ~10% strain (Supplementary Figs. 36 and 37). Hence, these trivial strain distortions suggest that local structural distortions adjacent to the defect centre play important roles in tuning the magnetic moments. Consequently, the non-magnetic TMDC system exhibits magnetism due to bonds broken originating from metal vacancies-induced local strain across the nearest and next-nearest X/M atoms.
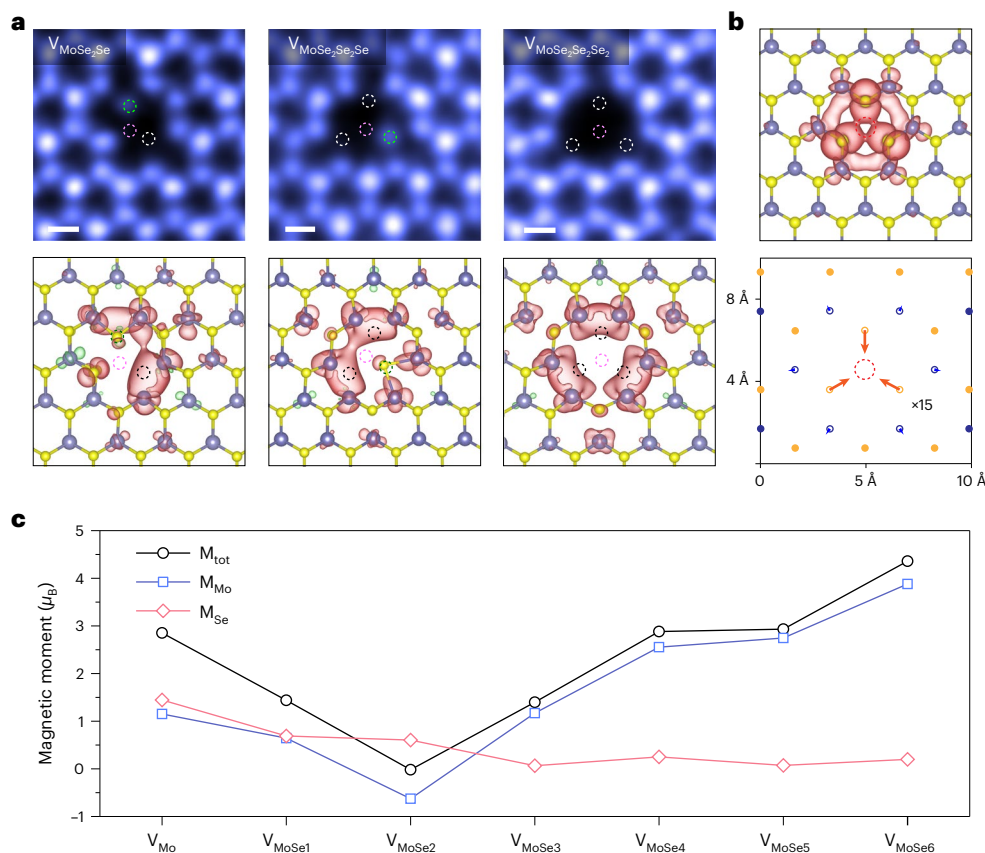
Fig. 4 | DFT-calculated electronic properties of metal vacancy complexes in MoSe₂ monolayer. a, Spin-density distribution (bottom) of V_{MoSe_2Se}, $V_{MoSe_2Se_2Se}$ and $V_{MoSe_2Se_2Se_2}$ vacancy complexes, deduced from experimental images (top), in monolayer MoSe₂. Purple and yellow balls represent Mo and Se atoms, respectively. The position of the missing Mo, one Se, and double Se atoms are highlighted by pink, green and white/black dashed circles. The red and green isosurfaces correspond to spin-up and spin-down charge densities. **b**, Spin-density distribution (top) at V_{Mo} defect and corresponding atom coordinate changes (bottom). The arrows denote the displacement vectors multiplied by 15 times for visualization. **c**, Evolution of magnetic moments for $V_{MoSe_{0-6}}$, where the total (M_{tot}) and local magnetic moments from adjacent Mo (M_{Mo}) and Se (M_{Se}) atoms are illustrated. Scale bars: 0.2 nm (**a**).

Conclusions

In conclusion, our results present a generic atom manipulation approach to fabricating various metal vacancies in an atlas of monolayer TMDCs. An e-beam–matter interaction, the chemical-induced knock-on effect, is demonstrated to be mainly responsible for the selective engineering metal vacancies in TMDC monolayers as atomically unveiled and suggested by combined STEM imaging and DFT calculations. Upon continuous e-beam bombardments, metal vacancies gradually grow in an atom-by-atom manner, consecutively losing neighbouring chalcogen and metal atoms, accompanied by the self-healing process. As suggested by DFT, the local magnetic moment can reach 2.85 μ_B and 4.36 μ_B in V_{Mo} and $V_{MoSe_2Se_2Se_2}$ in monolayer MoSe₂ due to the unpaired Se p and Mo d electrons highly related to local lattice distortions induced by metal vacancies. Therefore, our systematic investigation of metal vacancies marks a step forward for collectively engineering atoms located at the interior atomic plane via a synergetic electron–matter interaction and paves a promising way to achieve desired exotic functionalities in atomically thin 2D materials via atom engineering.

Methods

PVP-assisted electrochemical exfoliation

Electrochemical exfoliation of TMDCs was carried out using an electrochemical workstation (CHI760E) with a two-electrode system as has been recently reported[33]. Two-dimensional TMDC bulk crystals and a Pt wire served as the cathode and counter electrode, respectively, and 0.001 M tetrahexylammonium chloride (THA·Cl, Sigma-Aldrich) in propylene carbon and 1.0 g L⁻¹ PVP (molecular weight 55,000 g mol⁻¹, Sigma-Aldrich) in dimethylformamide (DMF) are mixed as the electrolyte. The constant negative voltage of −3 V to −5 V was applied to drive the intercalation of ammonium cations into bulk crystals, resulting in gentle expansion and exfoliation. The as-exfoliated TMDC flakes were separated and collected by centrifugation followed by repeated washing with DMF. The as-produced TMDC/DMF (or water) solution was dropped onto a holey carbon transmission electron microscopy (TEM) substrate for TEM observation.

E-beam-induced metal vacancies

Suspended monolayer TMDCs flakes were irradiated with e-beam accelerated by 60 kV using Nion U-HERMES200 microscope. The beam current was ~15 pA, and the per-pixel dwell time was 8 μs, while beam intensity was adjusted to realize the continuous change of irradiation doses. The concentration of point defects was controllable by tuning irradiation doses and time.

STEM characterization

ADF-STEM imaging was performed on an aberration-corrected Nion U-HERMES200, equipped with a cold field emission gun. The accelerating voltage was 60 kV, below the knock-on damage threshold of all the TMDs studied in this work. The convergence semiangle of the probe was around 35 mrad. The collection angle for high-angle ADF and medium-angle ADF imaging was between 80 and 200 mrad and 30

to 110 mrad, respectively. Medium-angle ADF images were primarily used for imaging low Z atomic number atoms, especially in 1H-NbS$_2$, 1H-MoS$_2$, 1H-MoSe$_2$, 1T-TaS$_2$, 1H-TaSe$_2$ and 1T''-ReS$_2$. ADF-STEM images were filtered by Gaussian filters, and the positions of atomic columns were located by finding the local maxima of the filtered series. EDS were collected and processed in a probe-corrected JEOL ARM200F operating at 80 kV.

Deep learning

We trained FCNs[38] using simulated data generated via incoherent image simulations using abTEM[44]. To make the simulations more realistic, we apply a cycle generative adversarial network (CycleGAN)[45] that introduces a novel reciprocal space discriminator to augment the simulated data with realistic, complex spatial frequency information learned from experimental data. This approach generates our final training data with nearly indistinguishable images from real experimental data, while also providing labels for further deep-learning applications. The code information for FCNs, image simulations and CycleGAN are provided in the relevant reference.

DFT calculations

DFT calculations were performed using the generalized gradient approximation for the exchange-correlation potential, the projector augmented wave method[46,47], and a plane-wave basis set as implemented in the Vienna ab initio simulation package (VASP)[48,49]. We constructed defective configurations by introducing a $V_{M_m X_n}$ ($m = 0,1$; $n = 0$–6) in 6×6 supercells of monolayer MX$_2$ with a 20 Å vacuum space along the c axis. The kinetic energy cut-off for the plane-wave basis was 400 eV in all calculations. The criterion for total energy convergence was set to 10^{-4} eV and all atoms were allowed to relax until the residual force per atom was less than 0.02 eV Å^{-1}. A k-mesh of $3 \times 3 \times 1$ was adopted to sample the first Brillouin zone. Van der Waals interaction was considered at the DFT-D3 level with the Perdew–Burke–Ernzerhof functional[50,51]. For 1H-NbS$_2$ defective systems, on-site Coulomb interactions were considered on the Nb d orbitals with an effective value $U = 3.2$ eV, which was estimated using a linear-response method[52]. The formation energy was defined as $E_{form} = E_{defect} - E_{pristine} + n \times \mu_{remove}$, where μ_{remove} is the chemical potential of the removed atoms to form a vacancy. We use $\mu_M^\star + 2\mu_X^\star \approx \mu_{MX_2}$ to calculate the chemical potentials, where the $\mu_M^\star(\mu_X^\star)$ is the chemical potential of M (X) in the bulk form. The range of them can be deduced as: $\mu_{MX_2} - 2\mu_X^\star \leq \mu_M \leq \mu_M^\star$, $\frac{1}{2}(\mu_{MX_2} - \mu_M^\star) \leq \mu_X \leq \mu_X^\star$. Note that μ_{MX_2} can be taken as the total energy per one formula unit of 2D MX$_2$. An initial magnetic moment of 3 μB was set on each atom. Two types of magnetic exchange were considered, including antiferromagnetic and ferromagnetic, in the survey of the magnetism of defective monolayer TMDCs.

Data availability

All data are available in the main text or Supplementary Information. Source data are provided with this paper.

References

1. Crommie, M. F., Lutz, C. P. & Eigler, D. M. Confinement of electrons to quantum corrals on a metal. *Surf. Sci.* **262**, 218–220 (1993).
2. Khajetoorians, A. A. et al. Atom-by-atom engineering and magnetometry of tailored nanomagnets. *Nat. Phys.* **8**, 497–503 (2012).
3. Khajetoorians, A. A., Wegner, D., Otte, A. F. & Swart, I. Creating designer quantum states of matter atom-by-atom. *Nat. Rev. Phys.* **1**, 703–715 (2019).
4. Gomes, K. K., Mar, W., Ko, W., Guinea, F. & Manoharan, H. C. Designer Dirac fermions and topological phases in molecular graphene. *Nature* **483**, 306–310 (2012).
5. Drost, R., Ojanen, T., Harju, A. & Liljeroth, P. Topological states in engineered atomic lattices. *Nat. Phys.* **13**, 668–671 (2017).
6. Slot, M. R. et al. Experimental realization and characterization of an electronic Lieb lattice. *Nat. Phys.* **13**, 672–676 (2017).
7. Kempkes, S. N. et al. Design and characterization of electrons in a fractal geometry. *Nat. Phys.* **15**, 127–131 (2019).
8. Eigler, D. M. & Schweizer, E. K. Positioning single atoms with a scanning tunnelling microscope. *Nature* **344**, 524–526 (1990).
9. Song, Y. J. et al. High-resolution tunnelling spectroscopy of a graphene quartet. *Nature* **467**, 185–189 (2010).
10. Dyck, O. et al. Atom-by-atom fabrication with electron beams. *Nat. Rev. Mater.* **4**, 497–507 (2019).
11. Sergei, V., Kalinin, Borisevich, A. & Jesse, S. Fire up the atom forge. *Nature* **539**, 485–487 (2016).
12. Huang, P. Y. et al. Imaging atomic rearrangements in two-dimensional silica glass: watching silica's dance. *Science* **342**, 224–227 (2013).
13. Lin, J. et al. Flexible metallic nanowires with self-adaptive contacts to semiconducting transition-metal dichalcogenide monolayers. *Nat. Nanotechnol.* **9**, 436–442 (2014).
14. Zhao, X. et al. Atom-by-atom fabrication of monolayer molybdenum membranes. *Adv. Mater.* **30**, 1707281 (2018).
15. Zhou, W. et al. Intrinsic structural defects in monolayer molybdenum disulfide. *Nano Lett.* **13**, 2615–2622 (2013).
16. Lin, J., Pantelides, S. T. & Zhou, W. Vacancy-induced formation and growth of inversion domains in transition-metal dichalcogenide monolayer. *ACS Nano* **9**, 5189–5197 (2015).
17. Parto, K., Azzam, S. I., Banerjee, K. & Moody, G. Defect and strain engineering of monolayer WSe2 enables site-controlled single-photon emission up to 150 K. *Nat. Commun.* **12**, 3585 (2021).
18. Liu, X. et al. Top-down fabrication of sub-nanometre semiconducting nanoribbons derived from molybdenum disulfide sheets. *Nat. Commun.* **4**, 1776 (2013).
19. Feng, Q. et al. Exploring atomic defects in molybdenum disulphide monolayers. *Nat. Commun.* **6**, 6293 (2015).
20. Zhang, Q., Wee, A. T. S., Liang, Q., Zhao, X. & Liu, M. Defect engineering of two-dimensional transition-metal dichalcogenides: applications, challenges, and opportunities. *ACS Nano* **15**, 2165–2181 (2021).
21. Komsa, H. P. et al. Two-dimensional transition metal dichalcogenides under electron irradiation: defect production and doping. *Phys. Rev. Lett.* **109**, 035503 (2012).
22. Cho, S. et al. Phase patterning for ohmic homojunction contact in MoTe$_2$. *Science* **349**, 625–628 (2015).
23. Moody, G. et al. Microsecond valley lifetime of defect-bound excitons in monolayer WSe$_2$. *Phys. Rev. Lett.* **121**, 57403 (2018).
24. Schuler, B. et al. Large spin–orbit splitting of deep in-gap defect states of engineered sulfur vacancies in monolayer WS$_2$. *Phys. Rev. Lett.* **123**, 76801 (2019).
25. Mitterreiter, E. et al. The role of chalcogen vacancies for atomic defect emission in MoS$_2$. *Nat. Commun.* **12**, 3822 (2021).
26. Wang, X. et al. Vacancy defects in 2D transition metal dichalcogenide electrocatalysts: from aggregated to atomic configuration. *Adv. Mater.* **35**, e2206576 (2023).
27. Li, G. et al. All the catalytic active sites of MoS$_2$ for hydrogen evolution. *J. Am. Chem. Soc.* **138**, 16632–16638 (2016).
28. Wang, G. et al. Engineering the crack structure and fracture behavior in monolayer MoS$_2$ by selective creation of point defects. *Adv. Sci.* **9**, 2200700 (2022).
29. Avsar, A. et al. Probing magnetism in atomically thin semiconducting PtSe$_2$. *Nat. Commun.* **11**, 4806 (2020).
30. Heiranian, M., Farimani, A. B. & Aluru, N. R. Water desalination with a single-layer MoS$_2$ nanopore. *Nat. Commun.* **6**, 8616 (2015).
31. Yang, J. et al. Single atomic vacancy catalysis. *ACS Nano* **13**, 9958–9964 (2019).
32. Egerton, R. F. Radiation damage to organic and inorganic specimens in the TEM. *Micron* **119**, 72–87 (2019).

33. Yu, W. et al. High-yield exfoliation of monolayer 1T'-MoTe$_2$ as saturable absorber for ultrafast photonics. *ACS Nano* **15**, 18448–18457 (2021).

34. Nguyen, E. P. et al. Electronic tuning of 2D MoS$_2$ through surface functionalization. *Adv. Mater.* **27**, 6225–6229 (2015).

35. Chu, X. S. et al. Direct covalent chemical functionalization of unmodified two-dimensional molybdenum disulfide. *Chem. Mater.* **30**, 2112–2128 (2018).

36. Krivanek, O. L. et al. Atom-by-atom structural and chemical analysis by annular dark-field electron microscopy. *Nature* **464**, 571–574 (2010).

37. Meyer, J. C. et al. Accurate measurement of electron beam induced displacement cross sections for single-layer graphene. *Phys. Rev. Lett.* **108**, 196102 (2012).

38. Lee, C. H. et al. Deep learning enabled strain mapping of single-atom defects in two-dimensional transition metal dichalcogenides with sub-picometer precision. *Nano Lett.* **20**, 3369–3377 (2020).

39. Selhorst, R. et al. Precision modification of monolayer transition metal dichalcogenides via environmental e-beam patterning. *ACS Nano* **17**, 2958–2967 (2023).

40. Zhu, Y. et al. Anisotropic point defects in rhenium diselenide monolayers. *iScience* **24**, 103456 (2021).

41. Niu, K. et al. Direct visualization of large-scale intrinsic atomic lattice structure and its collective anisotropy in air-sensitive monolayer 1T'-WTe$_2$. *Adv. Sci.* **8**, 2101563 (2021).

42. Cenker, J. et al. Reversible strain-induced magnetic phase transition in a van der Waals magnet. *Nat. Nanotechnol.* **17**, 256–261 (2022).

43. Yang, F. et al. Emerging enhancement and regulation strategies for ferromagnetic 2D transition metal dichalcogenides. *Adv. Sci.* **10**, 2300952 (2023).

44. Madsen, J. & Susi, T. The abTEM code: transmission electron microscopy from first principles. *Open Res. Eur.* **1**, 24 (2021).

45. Khan, A., Lee, C. H., Huang, P. Y. & Clark, B. K. Leveraging generative adversarial networks to create realistic scanning transmission electron microscopy images. *NPJ Comput. Mater.* **9**, 85 (2023).

46. Blöchl, P. E. Projector augmented-wave method. *Phys. Rev. B* **50**, 17953–17979 (1994).

47. Kresse, G. & Joubert, D. From ultrasoft pseudopotentials to the projector augmented-wave method. *Phys. Rev. B* **59**, 1758–1775 (1999).

48. Kresse, G. & Furthmüller, J. Efficient iterative schemes for ab initio total-energy calculations using a plane-wave basis set. *Phys. Rev. B* **54**, 11169–11186 (1996).

49. Kresse, G. & Furthmüller, J. Efficiency of ab-initio total energy calculations for metals and semiconductors using a plane-wave basis set. *Comput. Mater. Sci.* **6**, 15–50 (1996).

50. Grimme, S., Antony, J., Ehrlich, S. & Krieg, H. A consistent and accurate ab initio parametrization of density functional dispersion correction (DFT-D) for the 94 elements H–Pu. *J. Chem. Phys.* **132**, 154104 (2010).

51. Grimme, S. Semiempirical GGA-type density functional constructed with a long-range dispersion correction. *J. Comput. Chem.* **27**, 1787–1799 (2006).

52. Cococcioni, M. & De Gironcoli, S. Linear response approach to the calculation of the effective interaction parameters in the LDA+U method. *Phys. Rev. B* **71**, 035105 (2005).

Author contributions

X.Z. and J. Zhang conceived and designed the experiments. X.H. and Y.L. synthesized materials and performed the STEM characterizations. M.N. and J.Q. built the theoretical model and performed DFT calculations. X.H., M.N. and Y.L. conducted all analysis under the supervision of J.Q., J. Zhang and X.Z. R.L., J.D., X.W., A.V.T., W.J., Y.W. and J. Zhou contributed to the sample measurements and mechanism understanding. Y.H. conducted deep deep-learning experiment. X.H., M.N., J.Q. and X.Z. co-wrote the manuscript. All the authors discussed the results and contributed to preparing the manuscript.

Competing interests

The authors declare no competing interests.

Additional information

Supplementary information The online version contains supplementary material available at https://doi.org/10.1038/s44160-024-00501-z.

Correspondence and requests for materials should be addressed to Jingsi Qiao, Jin Zhang or Xiaoxu Zhao.

Peer review information *Nature Synthesis* thanks Marijn van Huis and the other, anonymous, reviewer(s) for their contribution to the peer review of this work. Primary handling editor: Alexandra Groves, in collaboration with the *Nature Synthesis* team.

Reprints and permissions information is available at www.nature.com/reprints.